



The 2022 Goesan earthquake of the moment magnitude 3.8 along the buried fault in the central Korean Peninsula

Hobin Lim · Chang Soo Cho ·
Minkyung Son

Received: 18 October 2023 / Accepted: 22 February 2024 / Published online: 6 March 2024
© The Author(s) 2024

Abstract On October 28, 2022, a moment magnitude (M_w) 3.8 earthquake occurred in Goesan, South Korea, typically characterized as a stable continental region. Herein, we analyze 42 earthquakes, including the M_w 3.8 earthquake, the largest foreshock (M_w 3.3), which preceded the mainshock by 17 s, and the largest aftershock (M_w 2.9). The primary aim of this study is to identify interactions among the seismic events. To this end, we utilized the permanent seismic networks with the closest station at 8.3 km from the epicenter, and the temporary network deployed eight

hours after the mainshock's occurrence. Relocation results delineate that the mainshock occurred at the southeastern tip of the hypocenter distribution of three foreshocks, trending west-northwest–east-southeast. The aftershocks form an overall spatially diffused seismic pattern that propagates toward both ends of the inferred lineament in the downdip direction. The rupture directivity of the mainshock, along with waveform similarity across the mainshock and foreshocks, confirms the inferred geometry, corresponding well with the focal mechanisms of the mainshock and the largest foreshock. We demonstrate that the change in Coulomb failure stress (ΔCFS) by the largest foreshock was positive where the mainshock occurred and that the mainshock generated ΔCFS capable of triggering the propagation of the aftershocks.

Highlights

- The 2022 Goesan earthquake (M_w 3.8) was preceded by the M_w 3.3 event in ~17s.
- This study determined how one seismic event influenced the next event in stable continental regions.
- The M_w 3.3 foreshock generated enough stress to trigger the mainshock along the buried fault.

Supplementary Information The online version contains supplementary material available at <https://doi.org/10.1007/s10950-024-10201-y>.

H. Lim · C. S. Cho · M. Son (✉)
Earthquake Research Center, Korea Institute of Geoscience and Mineral Resources, 124 Gwahak-ro, Yuseong-gu, Daejeon 34132, Republic of Korea
e-mail: kersti@kigam.re.kr

H. Lim
e-mail: HBL@kigam.re.kr

C. S. Cho
e-mail: nemex@kigam.re.kr

Keywords Stable continental region · Earthquake interaction · Coulomb failure stress · Waveform similarity · Foreshock · Aftershock

1 Introduction

On October 28, 2022, at 23:27:50 UTC, a moment magnitude (M_w) 3.8 earthquake occurred in the town of Goesan in the central region of South Korea (Fig. 1); there have been no reports of casualties or significant damage caused by the mainshock. The Korea Meteorological Administration (KMA) reported its local magnitude as 4.1. This region had

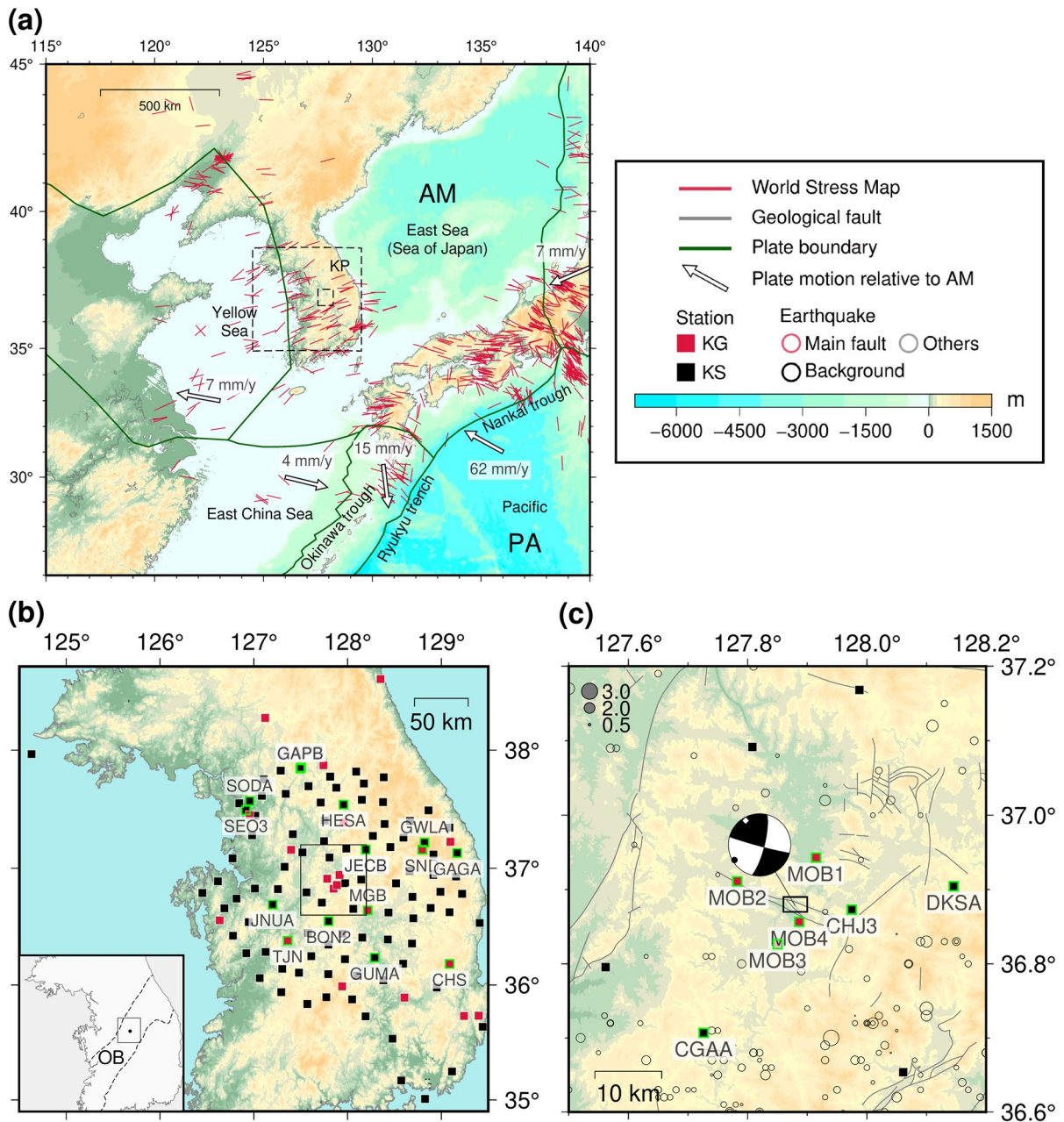


Fig. 1 Distribution of the Goesan earthquakes and tectonic setting. **a** Maximum horizontal crustal stress with the tectonic setting around the Korean Peninsula. Stress is obtained from the World Stress Map (Heidbach et al. 2018). Plate boundary is from Bird (2003). Larger and smaller dashed boxes indicate regions of (b) and (c), respectively. **b** Stations used in this study. Inset shows the geological province, Okcheon Belt (OB), including the epicenters. The box indicates the region of (c). **c** Magnified map including the stations used to determine

hypocenters. The box indicates the region of the map view in Fig. 5a. The background seismicity in 1978–2022 is plotted (seismicity from ‘<https://necis.kma.go.kr>’ accessed on 31 July 2023). The geological faults are from ‘<https://doi.org/10.22747/data.20230712.5013>’ (accessed on 2 May 2023). AM: Amurian Plate. PA: Pacific Plate. JF: Jogok Fault (Park 2005). KG: Korea Institute of Geoscience and Mineral Resources. KS: Korea Meteorological Administration. KP: Korean Peninsula

no reported destructive earthquakes since 1978, when modern seismic monitoring was initiated.

The Korean Peninsula is located in stable continental regions with a relatively uniform ambient stress field in South Korea (Fig. 1a). The direction of the maximum horizontal compressional stress axis in inland South Korea is east-northeast–west-southwest (Fig. 1a). The region of the epicenter was within the Okcheon Belt, a geological province in South Korea, approximately 1,000 km from the closest Nankai Trough in Japan (Fig. 1a and b).

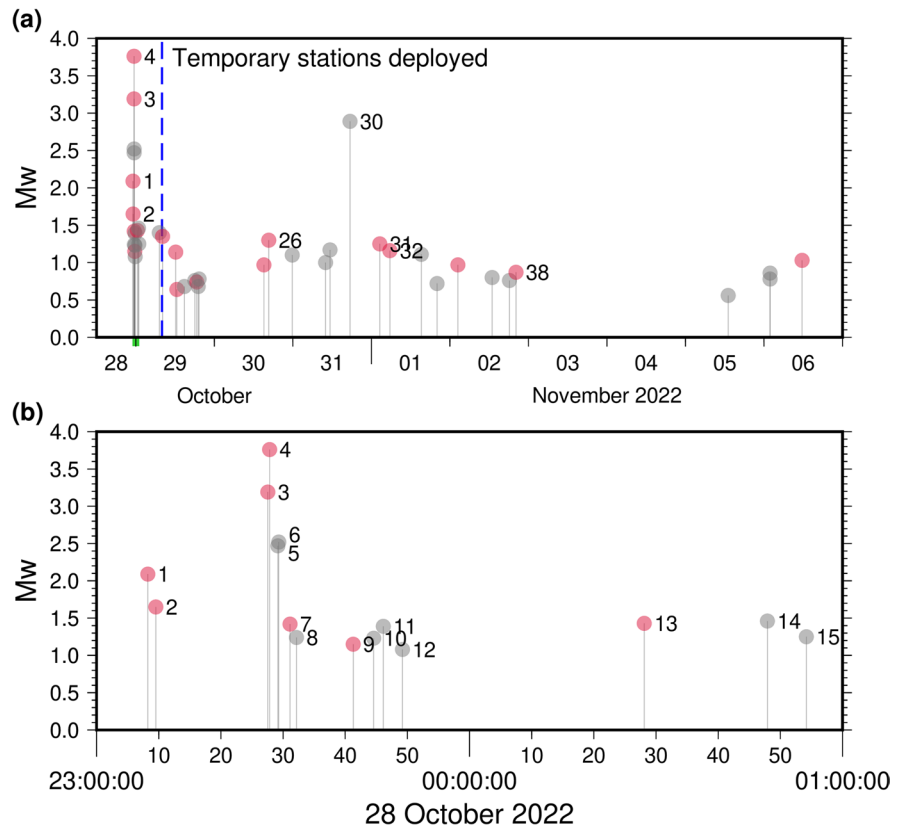
Geological faults, including the Jogok Fault (JF), are located in the region (Fig. 1c). The JF is subparallel to the strike of the mainshock’s nodal plane, with a maximum deviation of 10° (Fig. 1c). The main sense of slip across the JF is left-lateral (Park 2005), which is consistent with the focal mechanism of the mainshock (Fig. 1c). However, the lack of seismicity between the surface and subsurface at a focal depth of ~ 10 km limits further analysis.

Notably, the mainshock was preceded by a Mw 3.3 foreshock that occurred at 23:27:33 on October

28, 2022 (UTC), approximately 17 s before the mainshock (events 3 and 4 in Fig. 2). Permanent stations recorded the largest foreshock’s S-wave coda interfering with the P wave of the mainshock from a distance greater than ~ 135 km (Fig. 3). The Korea Institute of Geoscience and Mineral Resources deployed four temporary broadband stations within 10 km from the epicenter of the Mw 3.8 mainshock (see Fig. 1c). These stations began operation at 8:00:00 on October 29, 2022 (UTC), approximately eight hours after the mainshock occurred (see the dashed line in Fig. 2a) and recorded the largest aftershock of Mw 2.9 (event 30 in Fig. 2a).

This study utilized data from both the temporary and permanent stations to enhance constraints for locating hypocenters, complementing previous studies on the Goesan earthquakes (Hong et al. 2023; Kim et al. 2023; Sheen et al. 2023). We delved into possible interactions among the foreshock, mainshock, and aftershocks, precisely relocating hypocenters and examining whether a coseismic static stress model can account for the associated successive seismicity.

Fig. 2 Chronology of the earthquake sequence. **a** Period from October 28, 2022 to November 6, 2022. Red and grey circles represent events included in the main fault and others, respectively. A dashed line indicates the time when four temporary stations were deployed. **b** A magnified plot for a two-hour window, including events 1–15, as marked with a green tick on the time axis of (a)



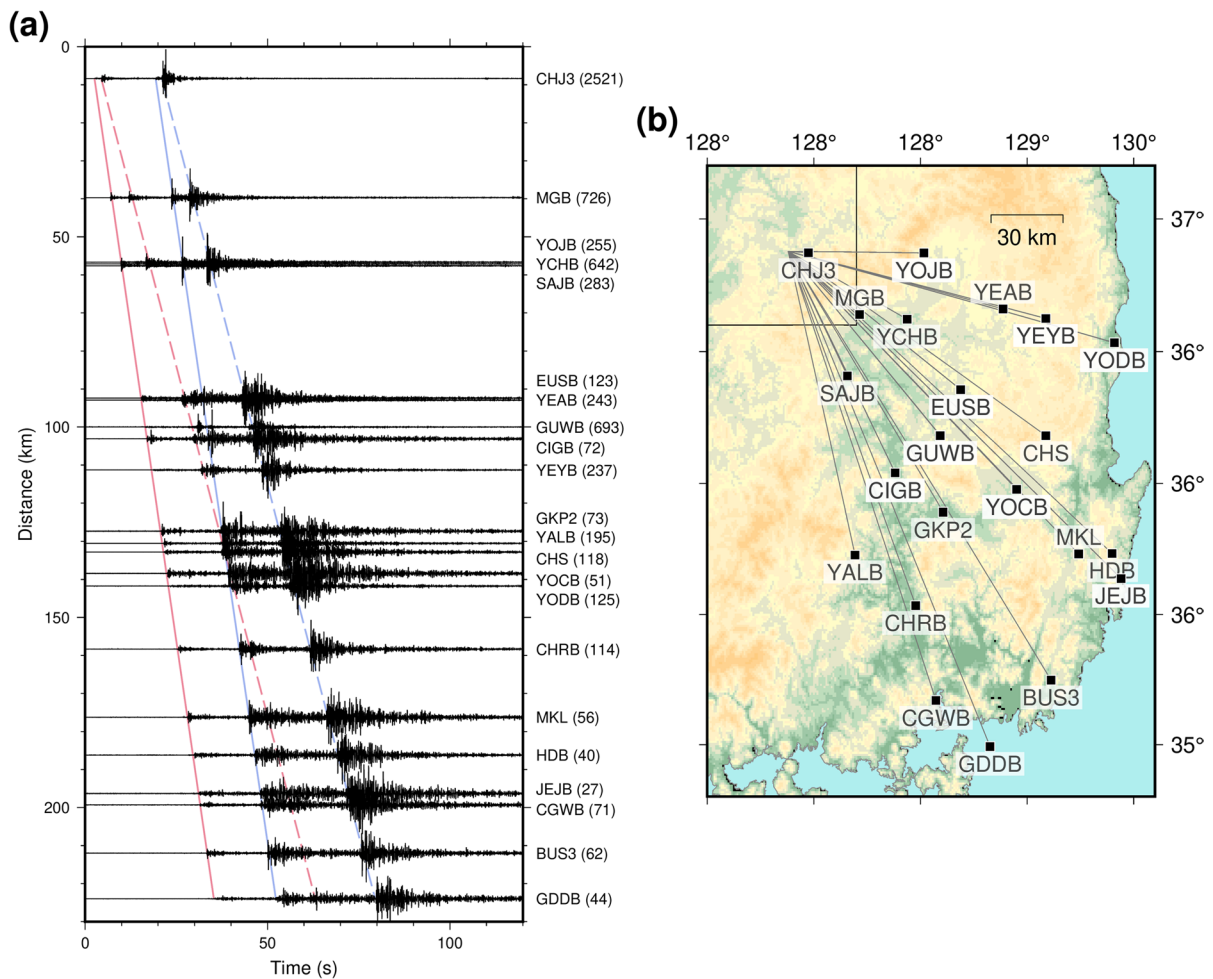


Fig. 3 Interference between the Mw 3.3 foreshock (event 3) and Mw 3.8 mainshock (event 4). **a** Vertical record sections of event 3 and event 4. Their difference in origin time is 17 s (Table 1). The trace is filtered in 2–8 Hz by acausal Butterworth of four poles. P and S wave arrivals are guided by solid and dashed lines, respectively. Faint red and blue lines are

events 3 and 4, respectively. The S waves of event 3 and the P waves of event 4 cross at ~135 km. The amplitude of the trace is normalized. Names of the stations are on the right, and the peak-to-peak amplitudes in $\mu\text{m/s}$ are within parentheses. The azimuth of the stations ranges from 90° to 170° . **b** Map of the station used in (a). A box in (b) indicates the region of Fig. 1c

This effort could contribute to a better understanding of earthquake triggering and interaction in stable continental regions.

2 Data and methods

2.1 Earthquake detection and relocation

We detected small-magnitude earthquakes using the template-matching method based on the list of 30 events provided by the KMA. From October 28 to

November 10, 2022, vertical components of seismic waveforms were band-pass filtered at 2–14 Hz for time window durations of -1 s to 3 s in terms of P wave at three stations, CHJ3, DKSA, and CGAA (Fig. 1c). We used waveforms with a mean correlation coefficient greater than 0.3.

Subsequently, P and S wave arrival times in the vertical and transverse components, respectively, were measured manually at 11 stations including the four temporary stations (Fig. 1c), to enhance relocation accuracy and decrease the minimum magnitude of locatable events. Manual measurement was

employed to prevent cyclic-skipping and undesirable effects resulting from varying durations (Bachura and Fischer 2019). The initial hypocenters were determined using *bayesloc* (Myers et al. 2007) with a 1-D velocity model for the Korean Peninsula based on the model described by Kim et al. (2022) originating from Kim and Kim (1983) (Table S1).

The double-difference method was applied to enhance the relative hypocenters based on the two sets of differential times (DT) for the P and S waves (Waldhauser and Ellsworth 2000). The first set comprised differential travel times of event pairs from P and S arrival picks (DT_1) while the second set was based on waveform cross-correlation (DT_2) after the waveform was interpolated to 1,000 samples per second. In the waveform cross-correlation, we used a short window from -0.015 s to 0.015 s in terms of P or S arrival picked manually. We only used the DT_2 if $|DT_2 - DT_1| < 0.01$ s to prevent cyclic-skipping and unintended effects caused by various durations. The 1,921 DT_1 helped to determine the overall distribution of the relative hypocenters; the 1,591 DT_2 fine-tuned the hypocenters.

Finally, the hypocenters were shifted by the absolute hypocenter of the largest aftershock (event 30), presumed to have the highest accuracy as it was recorded by the temporary stations. We estimated the uncertainty of the relative hypocenters through a bootstrapping approach. A total of 370 pairs were considered (Fig. S1 in the supplementary materials), with 70% (i.e., 259 pairs) randomly selected without duplication. The perturbed relocated hypocenters were shifted by the unperturbed absolute hypocenter of event 30, and this process was repeated 1,000 times.

2.2 Source spectrum fitting

We estimated the moment magnitude (M_w) and corner frequency (f_c) of earthquakes by fitting the S wave source spectrum with the Brune model (Brune 1970, 1971). The geometrical spreading and intrinsic attenuation were corrected to displacement source spectra, and the best-fitting model for the spectra was determined through a grid-searching scheme with an adopted range of domains and spacing (see details in Text S1 in the supplementary materials). The searching domain was set near the

initial values of M_w and f_c with the Snoke method (Snoke 1987; see details in Supplementary Text S2).

For the mainshock (event 4), we used data from 8 stations in distance of 116–325 km (see the list of stations in Table S2 in the supplementary materials). For the largest aftershock (event 30), we used more stations, up to 17, in distance of 39–397 km, because it was free from coda interferences caused by preceding large-sized events. However, for the largest foreshock (event 3), we had no other choice but to use the closest single station, CHJ3, at a distance of 8 km, due to the S coda interfering with the P wave of the mainshock (Fig. 3). This single measurement limited the reliability of the estimated f_c for event 3.

We employed the single-station approach using CHJ3 to estimate moment magnitudes for 40 earthquakes, which were events 1 to 3, 5 to 29, and 31 to 42. However, for event 30, we utilized 17 stations owing to the large amplitudes of the event, making it the largest aftershock.

2.3 Focal mechanism determination

We utilized the Time Domain Moment Tensor inversion tool (TDMT) (Dreger 2003; Minson and Dreger 2008) to derive moment tensor solutions for the M_w 3.8 mainshock (event 4) and M_w 3.3 foreshock (event 3), based on the velocity model of Kim et al. (2011) (Fig. S2 in the supplementary materials). However, for the foreshock (event 3), we only applied data from three stations (CHS, SND, and TJN) within limited time windows because the S wave of the foreshock and P wave of the mainshock interfered at distances > 135 km (see Fig. 3). For the mainshock (event 4), we applied data from 11 stations spanning a distance of 72–306 km. The applied passbands for the mainshock and foreshock were 0.04–0.10 Hz and 0.09–0.20 Hz, respectively. The passband for the mainshock was tuned by trial and error to minimize the interference effect of coda from the largest foreshocks. The centroid depth was assessed every 1 km between 1 and 17 km. (Fig. S2 in the supplementary materials). The focal mechanism of events 3 and 30 were determined based on P wave polarity in the vertical component, using *focmec* (Snoke 2003) (Fig. S3).

2.4 Rupture directivity estimation

We used unilateral and bilateral rupture models to assess an azimuthal dependency of f_C . The reciprocal of the f_C is the apparent source duration Δt (Brune 1970, 1971). In the unilateral model, the rupture propagated toward only one side laterally. In the bilateral model, the rupture propagated toward both sides with equal length and rupture velocity. The apparent source duration, Δt , can be modeled using Eqs. (1) and (2) for the unilateral and bilateral ruptures, respectively (Cesca et al. 2011).

$$\Delta t(AZ) = -A \cos(AZ - STK) + B \quad (1)$$

$$\Delta t(AZ) = A |\cos(AZ - STK)| + B \quad (2)$$

The AZ and STK stand for the azimuth to a station and the strike of the fault, respectively. The AZ is determined from the locations of the event and the station. Equations (1) and (2) assume that the fault has a lateral rupture direction with no vertical component. The A describes the fault's lateral width, L , with the relation $A = L/\beta$, where β represents the shear wave velocity (Cesca et al. 2011). Similarly, the B is defined as $B = t_r + L/V_R$, where t_r is the rise time, and V_R is the rupture velocity.

More general setups for rupture directivity, such as asymmetric bilateral rupture or involving the vertical component of the rupture direction, can be found in Cesca et al. (2011) and Park and Ishii (2015). However, we applied Eqs. (1) and (2) to our analysis, simplifying the fault rupture to consist solely of lateral directions. We aimed to determine the positive unknowns A and B through least-square linear inversion, using the four possible STK values. These values include opposing directions of a nodal plane. If either A or B becomes negative, we attempted another value for the STK .

2.5 Evaluation of change in the Coulomb failure stress

We also evaluated whether the changes in coseismic static stress of one earthquake induce subsequent earthquakes based on the concept of the change in the Coulomb Failure Stress (ΔCFS) (Lin and Stein

2004; Ree et al. 2021; Kim et al. 2022). A positive ΔCFS indicates that the stress change causes the following event to have the assumed strike, dip, and rake. Conversely, a negative ΔCFS means that the stress change prevents the following event from occurring. The region with the negative ΔCFS is typically called the “stress shadow” (Freed 2005). We calculated the second-order tensor stress fields changed by the Mw 3.3 foreshock (event 3) and the Mw 3.8 mainshock (event 4) using the *Coulomb 3* program (Lin and Stein 2004).

For the mainshock (event 4), we assigned the “source fault” mechanism with the strike, dip, and rake values of 105° , 87° , and 13° , respectively (listed in Table 2), obtained from moment tensor inversion. These parameters were also applied to the source fault for the largest foreshock (event 3), instead of employing its own moment tensor solution. The moment tensor inversion for event 3 employed only three stations (TJN, SND, and CHS) and consequently provided a solution with low variance reduction (54.8%) and a relatively high non-double-couple component (34%) (see the solution shown in Fig. S2).

The fault size was simplified as a square with widths of 0.18 km for event 3 (Mw 3.3) and 0.35 km for event 4 (Mw 3.8). The latter was based on f_C estimated in the source spectrum fitting. The f_C can be converted to the radius r_0 of a circular rupture model using $0.21\beta/f_C$, where β is the shear wave velocity (Madariaga 1976). We set β as 3.5 km/s. The size of square was determined to match the area of the corresponding circle. Changing the shape of rupture model was intended to simplify the calculation of *Coulomb 3*, which does not carry a physical meaning to make a change in interpretation. For event 3, as we were unable to obtain a reasonable f_C , the rupture area (r_0 of 0.1 km) was derived from the assumption that the earthquake has a stress drop of 30 MPa. This value is equal to the rounded-off stress drop of event 4 determined using its f_C .

The final procedure involved conversion from a stress tensor to a scalar, ΔCFS , in terms of the targeted focal mechanism defined by strike, dip, and rake, designated the “receiver fault.” We set Young's modulus, Poisson ratio, and effective frictional coefficient as 80 GPa, 0.25, and 0.4, respectively.

3 Results

3.1 Moment magnitude

We denote moment magnitudes that were estimated through the source spectrum fitting as M_w^B ('B' stands for Brune) and those estimated through the TDMT inversion as M_w^{TDMT} . The 42 earthquakes have M_w^B ranging from 0.6 to 3.8 (Table 1). The M_w^B of the mainshock (event 4) was same as the M_w^{TDMT} of it (M_w 3.8). The M_w^B and M_w^{TDMT} of the largest foreshock (event 3) had a slight difference by 0.1. (M_w^B 3.2 in Table 1; M_w^{TDMT} 3.3 in Table 2). We preferred the M_w^{TDMT} for event 3 because it was constrained by a larger number of stations, that is 3, compared to the M_w^B , which was based on the single station (CHJ3). The M_w^B of the largest aftershock (event 30) was 2.9. See Fig. S2 in the supplementary materials for the detailed results of the TDMT inversion for events 3 and 4. Also, see Fig. S4–S6 in the supplementary materials for source spectrum fittings of events 3, 4, and 30, respectively. The asymptotic value of the source spectrum model to 0 Hz directly refers to the seismic moment.

3.2 Corner frequency (f_C) and directivity

We observed azimuthal dependency in the reciprocal of f_C across 8 stations for event 4 and 17 stations for event 30 (Fig. 4). The f_C is known to be affected by the directivity of rupture propagation. The f_C^{-1} of event 4 were distributed having the maximum at 116° in azimuth (refer to station CHS for event 4 in Table S2; Fig. 4a). That is, the f_C^{-1} exhibited a single-lobe pattern in azimuth, implying a unilateral rupture that propagated toward the west-northwest (Fig. 4a). On the other hand, the f_C^{-1} of event 30 had two minima at 12° and 202° in azimuth (refer to stations KSA and BGD, respectively, in Table S2; Fig. 4b). The f_C^{-1} had a two-lobe pattern in azimuth with the two estimated maxima (Fig. 4b), which indicates that the rupture had elongated apparent durations toward both of the directions, the west-northwest–east-southeast. This describes a bilateral directivity along the fault strike. It is noteworthy that the estimated directivity constrains the fault plane of the two nodal planes

derived from the focal mechanism, not depending on the spatial distribution of relocated hypocenters.

For event 4 (mainshock), the representative f_C was 3.61 Hz, and for event 30, it was 9.0 Hz. These values were obtained as the reciprocal of the constant term (B^{-1}) from the best-fitting sinusoidal curves in Fig. 4a and b, respectively. The r_0 of the mainshock, obtained from the representative f_C , was 0.20 km. The corresponding stress drop $\Delta\sigma$ was calculated with $\Delta\sigma = 7M_0/16r_0^3$, where M_0 is the seismic moment (Eshelby 1957). The $\Delta\sigma$ of the mainshock was 29 MPa. Similarly, the r_0 and $\Delta\sigma$ of event 30 were 0.08 km and 20 MPa, respectively.

3.3 Fault attributable to the mainshock

The focal mechanism solutions of the M_w 3.3 foreshock (event 3) and M_w 3.8 mainshock (event 4) had coherent nodal planes, which are west-northwest–east-southeast vertical strike-slip faults with a dominant double-couple composition of the mainshock by 97% and the foreshock by 66% (Figs. 5a and S2; Table 2). Due to the small number of stations, we were unable to interpret the high non-double-couple composition of event 3 (Fig. S2 in the supplementary materials). Relocated hypocenters of events 1, 2, and 3 and the mainshock (event 4) constitute a plane with a horizontal direction that is consistent with the west-northwest–east-southeast nodal plane in the focal mechanisms of event 3 and the mainshock (Fig. 5a). Also, this nodal plane was consistent with the directivity observed in f_C to west-northwest (285° ; Fig. 4a). Lateral and vertical extension of this plane covered smaller events. All the events within this extended plane were labeled with 'm' standing for 'main fault' in Table 1. They were marked as red color in Fig. 5 to distinguish the other events which were not included in the main fault. The west-northwest–east-southeast trend was also confirmed in previous studies (Hong et al. 2023; Kim et al. 2023; Sheen et al. 2023). Double-couple component of the focal mechanism for event 3 was similar to that constrained with P wave polarity (Table 2).

Of the two nodal planes, the largest aftershock (event 30) could be attributed to a west-northwest–east-southeast plane. This plane is subparallel to the main fault (Figs. 5 and S6), and the rupture directivity of event 30 (Fig. 4b) also aligns the fault plane trending west-northwest–east-southeast. The dip of

Table 1 List of the earthquakes

Event	Origin time (UTC)	Latitude (°)	Longitude (°)	Depth (km)	M _w ^B	<i>f</i> _C (Hz)
1 ^m	2022–10–28T23:08:14.8	36.87916	127.87828	13.28	2.1 ^a	-
2 ^m	2022–10–28T23:09:32.4	36.87954	127.87683	12.99	1.7 ^a	-
3 ^m	2022–10–28T23:27:33.5	36.87896	127.87705	13.00	3.2 ^a	(15.93) ^a
4 ^m	2022–10–28T23:27:50.2	36.87813	127.87979	12.83	3.8	3.61
5	2022–10–28T23:29:09.7	36.88351	127.86890	13.23	2.5 ^a	-
6	2022–10–28T23:29:18.8	36.88029	127.88341	12.78	2.5 ^a	-
7 ^m	2022–10–28T23:31:07.1	36.87890	127.87740	12.87	1.4 ^a	-
8	2022–10–28T23:32:09.3	36.88101	127.87781	12.58	1.2 ^a	-
9 ^m	2022–10–28T23:41:16.6	36.87797	127.88326	12.64	1.2 ^a	-
10	2022–10–28T23:44:35.0	36.87601	127.86418	11.44	1.2 ^a	-
11	2022–10–28T23:46:07.5	36.87983	127.87941	13.24	1.4 ^a	-
12	2022–10–28T23:49:12.4	36.88012	127.87857	13.17	1.1 ^a	-
13 ^m	2022–10–29T00:28:06.3	36.88001	127.87248	13.32	1.4 ^a	-
14	2022–10–29T00:47:55.2	36.87969	127.88278	13.29	1.5 ^a	-
15	2022–10–29T00:54:10.9	36.88313	127.87572	13.64	1.3 ^a	-
16	2022–10–29T07:09:43.1	36.88073	127.87794	13.01	1.4 ^a	-
17 ^m	2022–10–29T08:09:30.8	36.87801	127.88154	13.16	1.4 ^a	-
18 ^m	2022–10–29T12:10:55.9	36.87902	127.88057	13.21	1.1 ^a	-
19 ^m	2022–10–29T12:33:44.1	36.87782	127.88207	13.16	0.6 ^a	-
20	2022–10–29T14:50:38.2	36.88006	127.87935	13.68	0.7 ^a	-
21	2022–10–29T18:03:51.6	36.88250	127.88011	13.51	0.8 ^a	-
22 ^m	2022–10–29T18:38:23.3	36.87812	127.88221	13.22	0.7 ^a	-
23	2022–10–29T19:05:16.7	36.88099	127.88088	13.74	0.7 ^a	-
24	2022–10–29T19:21:00.2	36.88172	127.88150	13.50	0.8 ^a	-
25 ^m	2022–10–30T15:09:27.0	36.87701	127.88725	12.60	1.0 ^a	-
26 ^m	2022–10–30T16:37:59.6	36.87922	127.87793	12.93	1.3 ^a	-
27	2022–10–30T23:49:07.3	36.87942	127.88131	13.12	1.1 ^a	-
28	2022–10–31T10:00:23.7	36.87455	127.88148	13.09	1.0 ^a	-
29	2022–10–31T11:22:22.7	36.87994	127.88190	12.70	1.2 ^a	-
30	2022–10–31T17:27:52.8	36.88053	127.87695	12.89	2.9	9.0
31 ^m	2022–11–01T02:35:16.9	36.87775	127.88298	13.20	1.3 ^a	-
32 ^m	2022–11–01T05:40:34.7	36.87764	127.88171	13.14	1.2 ^a	-
33	2022–11–01T15:15:24.6	36.88009	127.88301	12.83	1.1 ^a	-
34	2022–11–01T20:03:57.6	36.87895	127.88365	12.74	0.7 ^a	-
35 ^m	2022–11–02T02:26:50.8	36.87759	127.88410	13.71	1.0 ^a	-
36	2022–11–02T12:55:19.1	36.87471	127.87609	13.54	0.8 ^a	-
37	2022–11–02T18:13:09.0	36.87941	127.88125	12.95	0.8 ^a	-
38 ^m	2022–11–02T20:12:33.3	36.87834	127.88223	13.16	0.9 ^a	-
39	2022–11–05T13:04:43.9	36.87661	127.88089	12.97	0.6 ^a	-
40	2022–11–06T01:51:57.8	36.88445	127.87680	11.72	0.9 ^a	-
41	2022–11–06T01:52:32.7	36.88041	127.87939	12.86	0.8 ^a	-
42 ^m	2022–11–06T11:39:25.8	36.87560	127.89049	13.39	1.0 ^a	-

Numbers are assigned in chronological order. Superscript m: event constituting the main fault; *f*_C: corner frequency estimated by the source spectrum fitting. a: measured with the single station with high uncertainty

the aftershock (68°) was slightly gentler than that of the mainshock (87°; Table 2). The P-axis of the faulting mechanisms observed in Fig. 5a was similar to

the direction of the maximum horizontal principal stress of the crust in South Korea suggested by Soh et al. (2018).

Table 2 Source properties of events 3, 4, and 30

Event	Mw ^{TDMT}	Strike (°)	Dip (°)	Rake (°)	Centroid depth	DC	CLVD
3	3.3	109; 18	84; 83	7; 174	14 km	66%	34%
3	-	104; 196	80; 81	-9; -170	-	-	-
4	3.8	105; 14	87; 77	13; 177	14 km	97%	3%
30	-	111; 208	68; 73	-19; -203	-	-	-

The preferred nodal plane is provided first for the strike, dip, and rake. Focal mechanisms for events 3 and 4 were determined using Time Domain Moment Tensor inversion (TDMT, Dreger 2003; Minson and Dreger 2008; the first and third rows). The focal mechanisms of events 3 and 30 were determined based on P wave polarity (Snoke 2003; the second and fourth rows). DC and CLVD indicate components of double couple component and compensated linear vector dipole, respectively

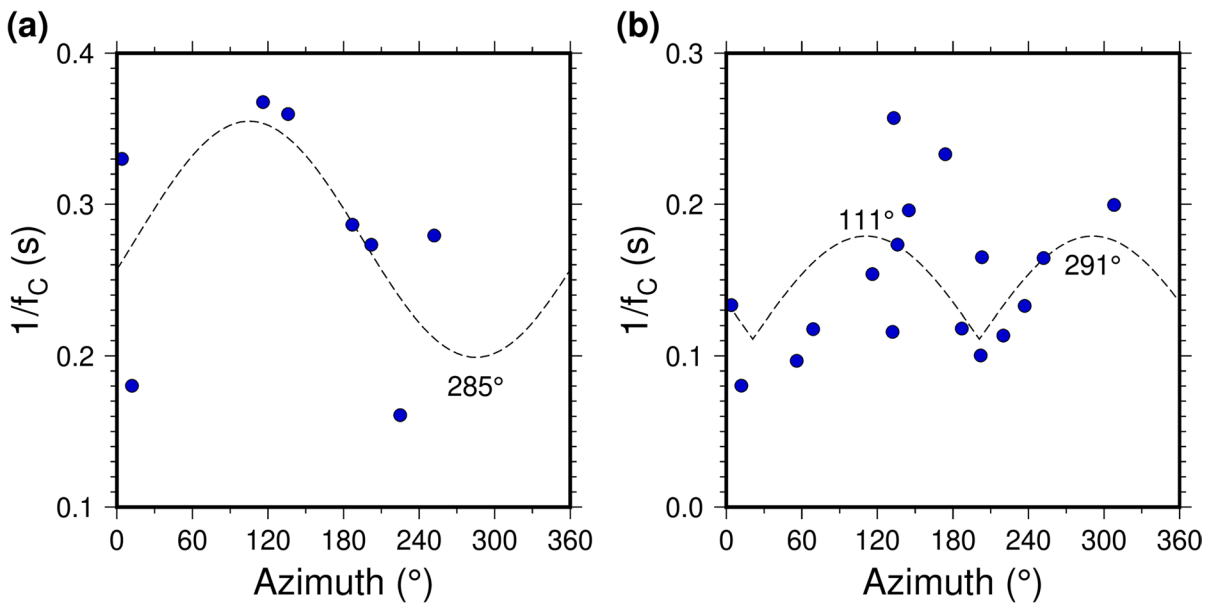


Fig. 4 Directivity of the mainshock and the largest aftershock. A reciprocal of f_C is plotted as a function of azimuth (AZ). **a** Mainshock (event 4) with unilateral rupture direction at 285° (west-northwest). **b** Largest aftershock (event 30) with bilateral rupture directions at 111° and 291° (west-northwest–east-southeast). The equations of the fitting

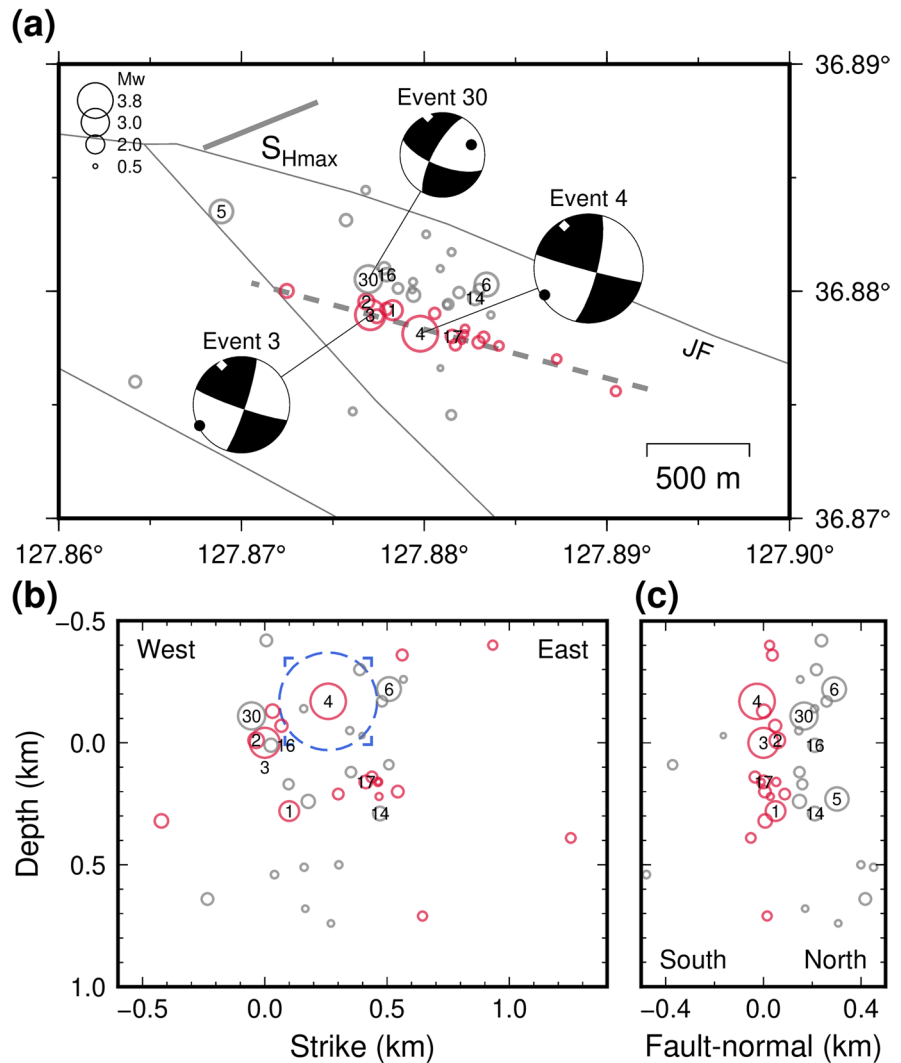
curves in **(a)** and **(b)** are $0.277 - 0.078\cos(AZ - 285^\circ)$ and $0.111 + 0.068|\cos(AZ - 111^\circ)|$, respectively. The equations were obtained with least-square linear regression with fixed azimuthal phases by 105° and 111° for event 4 and 30, respectively. The formulas for the curves representing rupture directivity were adopted from Cesca et al. (2011)

3.4 Changes in the Coulomb failure stress

We examined the spatiotemporal development of the Goesan earthquakes in terms of the coseismic static stress transfer using Δ CFSs. Figure 6 presents the Δ CFSs for the Mw 3.3 foreshock (event 3) and Mw 3.8 mainshock (event 4). The Δ CFS of the mainshock accumulated from the foreshock. The receiver fault was set to the strike, dip, and rake of the mainshock to assess the tendency for planar extension along the “main fault.”

The general patterns in Δ CFS include the presence of four positive lobes in the horizontal slice at a depth of 12.8 km (i.e., the focal depth of the mainshock; Fig. 6a; Table 1). Of these, two lobes were in the direction of both strikes, while the others were perpendicular. In detail, the mainshock (event 4) is within the positive zone induced by the largest foreshock (event 3) (Fig. 6a), indicating that the coseismic stress of the foreshock induced the mainshock. This remained valid when we considered the uncertainty of the location and the 3-D geometry in the vertical cross-section (Fig. 6b

Fig. 5 Results of the relocation and focal mechanism analysis for the Goesan earthquakes. **a** Map view of the relocated 42 earthquakes (open circles) and retrieved three fault plane solutions. S_{Hmax} is the maximum horizontal stress indicated by a thicker solid grey line (Soh et al. 2018). Red circle indicates events constituting the main fault (Table 1). **b** Fault-plane view. The cross-section is indicated by a dashed grey line in (a). Dashed circle indicates the rupture area with r_0 of 0.20 km for the Mw 3.8 mainshock (event 4). A square having the same area as that of the circle with width of 0.35 km for event 4 is indicated with four corners. The square-shaped fault is used in the analysis of ΔCFS . **c** Fault-parallel view. Origins in (b) and (c) are the coordinates of the largest foreshock (event 3; Mw 3.3) in Table 1



and c). Most of the perturbed epicenters by bootstrapping were included in the positive zone (Fig. 6b); the perturbed depths did not enter the negative zone in the cross-section (Fig. 6c). Similarly, Fig. 6d–f shows the horizontal and vertical slices of the ΔCFS with the perturbed locations of the aftershocks of the main fault (Table 1). The aftershocks were located in the positive zone in the vertical cross-section (Fig. 6f).

4 Discussion

4.1 Earthquakes following the static stress increase

We confirmed that the change in the coseismic static stress of the Mw 3.3 foreshock explained the occurrence of the mainshock (Fig. 6a). The occurrence of aftershocks was well understood based on the

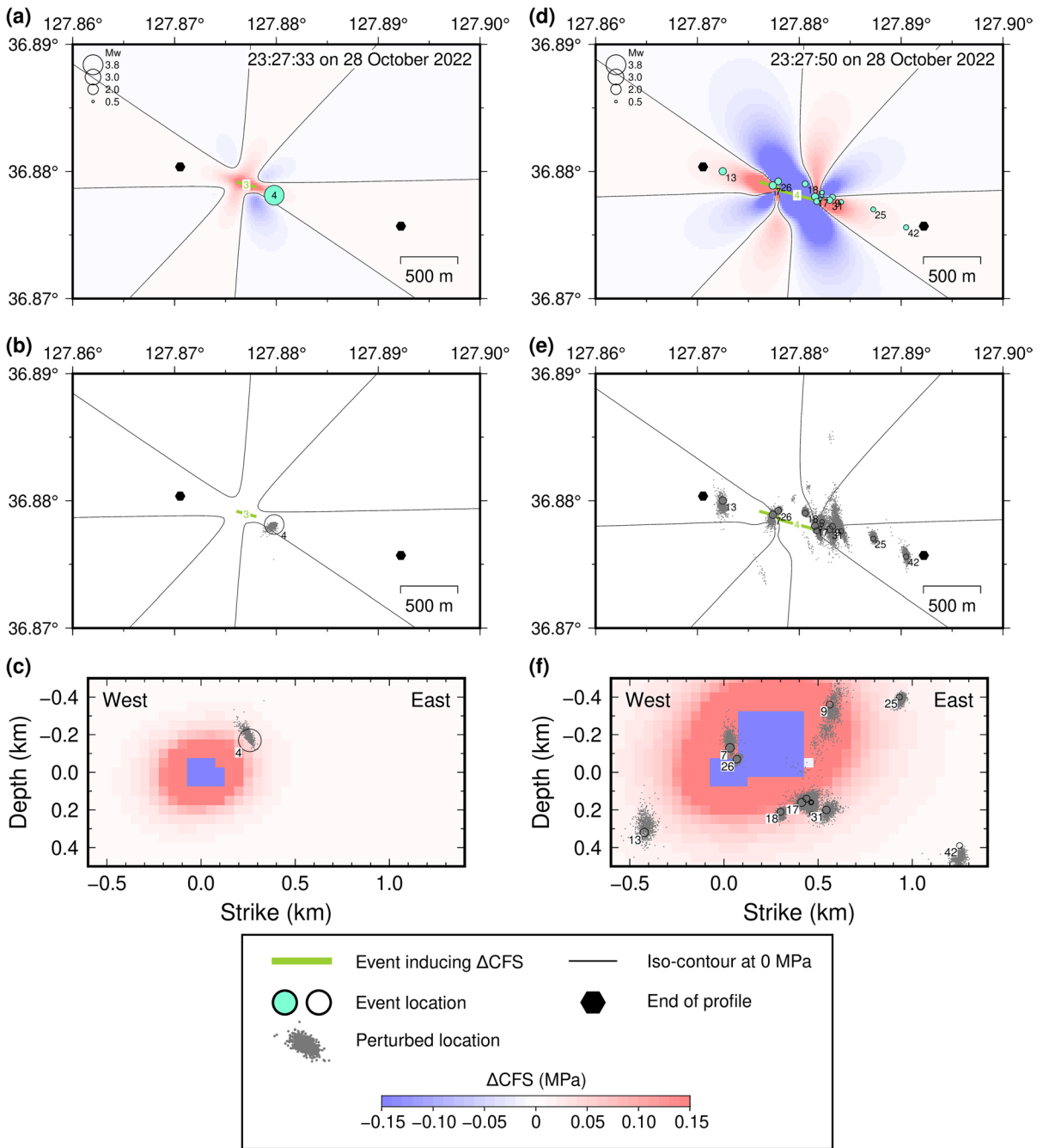


Fig. 6 Change in the Coulomb Failure Stress (Δ CFS) of the Mw 3.3 foreshock (event 3) and Mw 3.8 mainshock (event 4). The strike, dip, and rake of the receiver fault are 105°, 87°, and 13°, respectively. **a** Δ CFS of the Mw 3.3 foreshock. **b** Modified version from (a). Perturbed locations of the Mw 3.3 foreshock on the Δ CFS simplified by an iso-contour of 0 MPa. **c** Vertical cross-section of (a). **d** Δ CFS of the Mw 3.8 main-

shock added to the previous snapshot. The events within 100 m from the plane of the main fault, defined in Fig. 1, are only plotted. Time stamps in (a) and (d) indicate the origin times of the Mw 3.3 foreshock and Mw 3.8 mainshock, respectively (Table 1). **e** Modified version from (d), like (b), with the perturbed locations and the iso-contour of 0 MPa. **f** Vertical cross-section of (d)

cross-sectional view of the Δ CFS in the framework of the coseismic static stress (Fig. 6f). Events 7, 9, 17, 18, 26, and 31 were located near the edge of the rupture zone where the Δ CFS was highest (up to 0.15 MPa; Fig. 6f); although the upper limit near the rupture zone is sensitive to heterogeneous slip distribution, this was not determined in this study. Events 13, 25, and 42 were located relatively far from the rupture zone of the mainshock, extending the seismic zone to ~ 1.7 km horizontally and ~ 0.8 km vertically. Notably, this discussion presumes that the aftershocks had a similar focal mechanism as the mainshock.

4.2 The Mw 2.9 aftershock in the stress-shadow zone

The occurrence of the largest aftershock (event 30) in the negative Δ CFS zone is not simply explained in the Δ CFS (Fig. S7 in the supplementary materials). The applied stress tensor was the same as that for Fig. 6, however, the receiver fault was changed to the strike, dip, and rake of event 30. The epicenter of event 30 was at positive Δ CFS at the time of the largest foreshock (Fig. S7a in the supplementary materials); however, became negative at the time of the mainshock (Fig. S7b in the supplementary materials). Unlike other aftershocks in Fig. 6, event 30 does not conform to the 3-D geometry, mainly due to its depth of 12.89 km, a value close to the mainshock depth of 12.83 km (Table 1). However, we noticed that another study suggested that event 30 (event ‘25’ in their article) was located in the positive Δ CFS zone (Kim et al. 2023). The crucial distinction is in the depth of event 30, which differs from that of event 4 in their study by 0.6 km (hypocentral) or -1.5 km

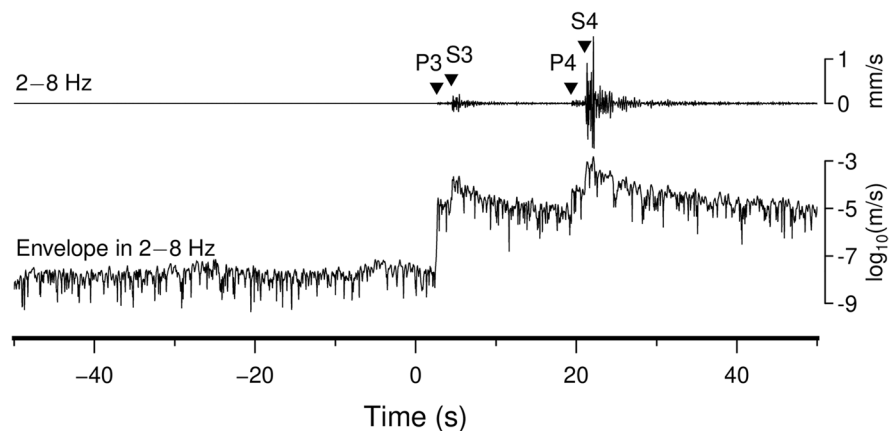
(centroid), while our results do not show this discrepancy. We also suggested alternative contributions to the occurrence of event 30: smaller events near event 30, such as event 16, could indicate a possible interaction between events 4 and 30 (Fig. 5). However, it is important to note that our understanding is limited, and further studies are needed to explore and validate these relationships. An oversimplified uniform rupture could be involved. Also, secondary mechanisms resulting from time-dependent changes in the frictional state can also affect the stress field (Dieterich 1994; Kilb et al. 2000; Freed 2005; Parsons 2005; Ree et al. 2021).

4.3 Limited implications from fore- and aftershocks

Foreshocks hold significant interest due to their potential role in triggering a mainshock; thus, it is crucial to comprehend the spatiotemporal features associated with their occurrence. Tape et al. (2018) found a notable observation that the high-frequency precursor in 2–8 Hz and the signal in the very low frequency band (0.02–0.05 Hz) are coincident within tens of seconds before the P arrival of the earthquake in central Alaska. However, we are unable to observe the high frequency precursor, following the same process as Tape et al. (2018). Traces filtered in the 2–8 Hz range and their log-scaled envelope in the top and bottom of Fig. 7 did not display any anomalous signal. The inspection for the wave in the very low frequency band is limited because of the short length of the window before the P arrival of the mainshock.

Waveform similarity can provide insights into the spatial feature of hypocenter distribution and

Fig. 7 Traces filtered in a high-frequency band. The station CHJ3’s vertical trace is filtered in 2–8 Hz at the top. P3 and S3 indicate the P and S wave arrival times of the Mw 3.3 foreshock (event 3); P4 and S4 are for the Mw 3.8 mainshock (event 4). The trace at the bottom is a log-scaled envelope from the top image to show the possible existence of a small amplitude precursor, which is absent in this figure



be applied to cross-check the relocation outcomes (Schaff and Richards 2004; Kim et al. 2010, 2022; Son et al. 2015, 2020; Sheen 2021). We assessed waveform similarity by computing cross-correlation coefficients (CCs) for the high-pass-filtered at 1 Hz in a 0–6 s window from the time of origin to include P wave arrival time and S coda. We used waveforms recorded by the north–south component of station CHJ3, positioned with an azimuth of 93°, nearly parallel to the transverse direction of ten events (1–6, 14, 16, 17, and 30). The selected events encompassed the three of foreshocks (events 1–3), relatively large-magnitude events (3–6, 14, 16, 17, and 30).

The CCs were grouped into two clusters: C1 comprised events 1–4, and 30, while C2 comprised events 5, 6, 14, 16, and 17 (Fig. 8a). Although the CC of event 6 was low and events 5 and 6 had negative polarity, we included them in C2 due to shared monochromatic features observed in each spectrum, similar

to those present in the spectra of other events (14, 16, and 17) in C2 (Fig. 8b and c). The low CC of event 6 was due to a slightly low-frequency peak at 27 Hz (Fig. 8c). The monochromatic feature with an average peak at ~29 Hz, after the S wave arrival (Fig. 8b and c) could result from a trapped mode in a fault zone (Li et al. 1990; Ben-Zion 1998; Li and Vernon 2001; Ross and Ben-Zion 2015). However, the exceptions observed in events 17 and 30, along with their opposite positions toward each group, are contradictory to this possibility.

Instead, we observed the spatial coherence among hypocenters in C1 and C2, except for events 17 and 30 in C2 and C1, respectively (see also Fig. 5). Events 1–4, constituting the main fault, were included in C1, whereas events 5, 6, 14, and 16 from C2 were not associated with the main fault. It is also noteworthy that C1 includes the foreshock-to-mainshock sequence (4 of 5), while C2 predominantly comprises

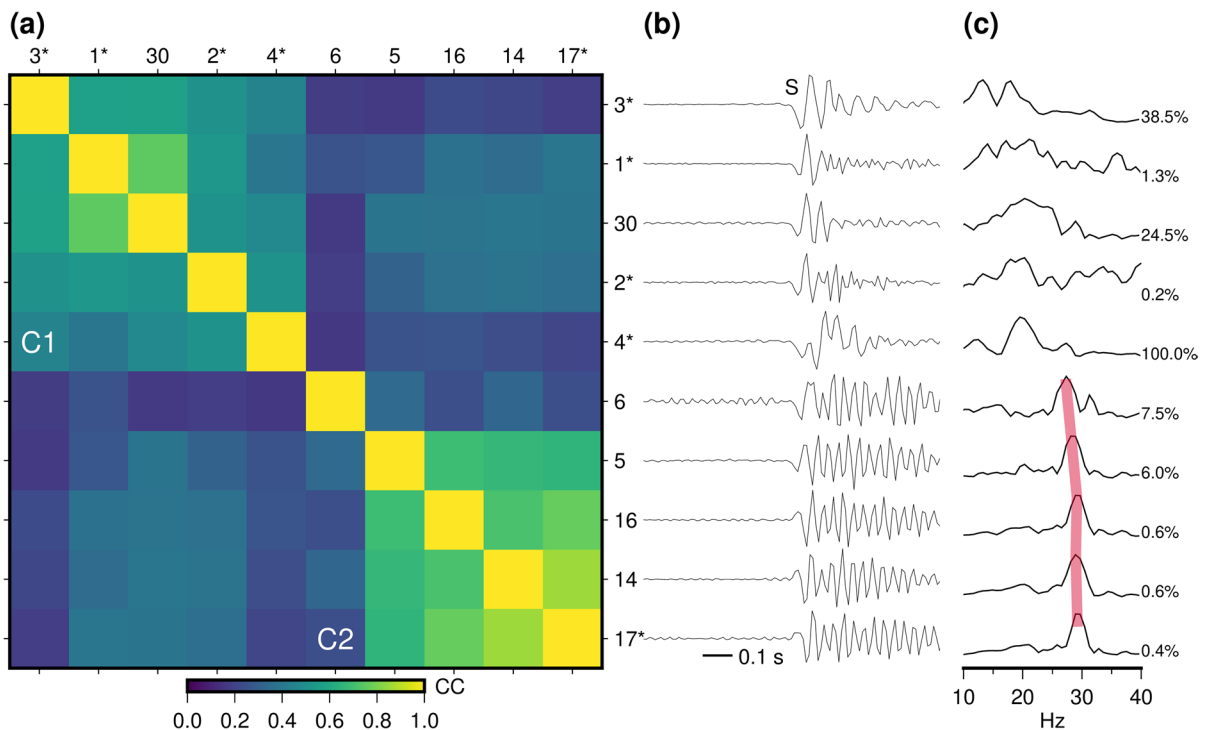


Fig. 8 Waveform similarity. **a** Cross-correlation (CC) matrix between the waveforms of station CHJ3 for the events labeled in Fig. 1. The events belonging to the main fault are marked by an asterisk. Cluster C1 comprises events 1–4, and 30, and C2 events 5, 6, 14, 16, and 17. **b** Transverse component aligned by the S arrival in a window from –0.5 to 0.5 s. The waveforms

are high-pass filtered at 1 Hz. The amplitude is normalized for visualization. **c** Spectra normalized in 10–40 Hz. The red line indicates peaks at ~29 Hz in the spectra of events 5, 6, 14, 16, and 17 having monochromatic phases after the S wave. The figure in percent in (c) indicates the relative scaling factor in terms of the peak amplitude of the mainshock

aftershocks. This observation may suggest the presence of structural or frictional heterogeneity at a local scale, indicating different faulting properties for each cluster within a relatively confined region around the main fault. The temporal distinction between foreshocks and aftershocks could further emphasize a possible mainshock-induced coseismic changes in the stress field of the confined region. This hypothesis needs additional waveform similarity analyses with more stations; however, we were not able to observe high-frequency waveform similarity at stations DKSA and CGAA, located relatively far from the epicenter to CHJ3, due to attenuated waveforms.

4.4 Coefficient A and stress drop ($\Delta\sigma$)

The A in Eq. (1) is described as $A = L/\beta$ where L is the fault's lateral width (Cesca et al. 2011). When we substituted A and β with 0.078 s and 3.5 km/s, respectively, L became 0.27 km, which was similar to the assumed square-shaped fault's width of 0.35 km in the calculation of the Δ CFS.

The $\Delta\sigma$ of 29 MPa for the mainshock (event 4) was larger than the average in the Korean Peninsula 1–10 MPa for Mw larger than 3.5 of Rhee and Sheen (2016). Also, the $\Delta\sigma$ was slightly larger than those of the 2016 Mw 5.5 Gyeongju earthquake, 11 MPa of Chai et al. (2020) based on the code wave, 13 MPa of Son et al. (2018) based on the Snoke method of S wave (Snoke 1987), and 23 MPa of Uchide and Song (2018) based on the finite fault inversion with the empirical Green's function method. Uchide and Song (2018) reported that the local $\Delta\sigma$ on the fault was up to 62 MPa. Caution must be applied when comparing the absolute values of stress drops that were estimated using different methods (Shearer et al. 2019; Abercrombie 2021; Calderoni and Abercrombie 2023).

5 Conclusions

The Mw 3.8 Goesan earthquake and its fore- and aftershocks represent a case with well-determined seismic properties owing to the dense national seismic networks and their geographical location in the central region of South Korea. Moreover, the rapid deployment of the temporary stations to provide azimuthal coverage within 10 km and one atop the mainshock epicenter improved the accuracy of the

foreshock, mainshock, and aftershock locations. Indeed, we shifted the hypocenters in terms of the coordinate of the largest aftershock that was determined through full utilization of the aftershock array.

The focal mechanisms of the mainshock and its largest foreshock (Mw 3.3; event 3) and aftershock (Mw 2.9; event 30) indicate a left-lateral strike-slip, of which the P-axis corresponds with the maximum horizontal axis of the current tectonic stress. The west-northwest–east-southeast trending strikes of the faulting mechanisms agree with the spatial distribution of the relocated hypocenters and the rupture directivity inferred from the azimuthal variation in corner frequency estimates obtained through source spectrum fitting. Based on the source spectrum fitting, we estimated the fault attributable to the mainshock. Its area of approximately 0.13 km² and the stress drop of 29 MPa.

The seismic properties identified the interaction between the mainshock and foreshock that preceded the mainshock by 17 s, as well as the development of most of the aftershock sequence. The mainshock occurred at the edge of the rupture zone, where the Δ CFS was positive. This indicates that the foreshock triggered the mainshock. Following the mainshock, the seismic zone propagated outside of the rupture zone. The cross-sectional view of the Δ CFS indicated that the aftershock distribution scattered horizontally and propagated downward from the rupture zone of the mainshock.

Acknowledgements We thank anonymous reviewers who gave helpful and thoughtful comments to improve the manuscript. Our appreciation also goes to Kwan-Hee Yun, Jeong-Ung Woo, Sunyoung Park, and Won-Young Kim for constructive discussion. We appreciate the Korea Meteorological Administration for providing seismic data. We would like to acknowledge efforts in the deployment of the aftershock monitoring array for the participants, I.S. Lim, S.H. Lee, K.S. Kim, H.M. Cho, H.I. Cho, Y.W. Yun, T.W. Kim, D.H. Lee, Y.J. Seong, and T.S. Oh. Also, we thank the earthquake monitoring team who provided early information on the earthquake. We thank the providers of the software, Generic Mapping Tools (Wessel et al. 2019), Seismic Analysis Code (Goldstein and Snoke 2005), Octave (<https://octave.org/>), Coulomb 3 (Lin and Stein 2004), and Inkscape (<https://inkscape.org/>).

Author contributions Hobin Lim: Conceptualization; Data curation; Software; Formal Analysis; Resources; Validation; Investigation; Visualization; Writing – original draft; Chang Soo Cho: Resources; Data curation; Software; Formal Analysis; Funding acquisition; Validation; Project administration; Writing – review & editing; Minkyung Son: Conceptualization;

Formal Analysis; Writing – original draft; Writing – review & editing.

Funding This study is supported by the Basic Research Project of Korea Institute of Geoscience and Mineral Resources.

Data availability The waveform data used in this study, including the cut and continuous data of the four temporary stations, can be found at <https://doi.org/10.5281/zenodo.7690346>. Continuous waveform data from the Korea Institute of Geoscience and Mineral Resources can be accessed at <https://data.kigam.re.kr/quake/> following approval. Continuous data from the Korea Meteorological Administration can be accessed at <https://necis.kma.go.kr/> following approval. The supplementary materials contain one table presenting the velocity model used to locate the hypocenters.

Code availability Codes used in this study will be shared upon reasonable request.

Declarations

Competing interests The authors declare no competing interests.

Open Access This article is licensed under a Creative Commons Attribution 4.0 International License, which permits use, sharing, adaptation, distribution and reproduction in any medium or format, as long as you give appropriate credit to the original author(s) and the source, provide a link to the Creative Commons licence, and indicate if changes were made. The images or other third party material in this article are included in the article's Creative Commons licence, unless indicated otherwise in a credit line to the material. If material is not included in the article's Creative Commons licence and your intended use is not permitted by statutory regulation or exceeds the permitted use, you will need to obtain permission directly from the copyright holder. To view a copy of this licence, visit <http://creativecommons.org/licenses/by/4.0/>.

References

- Abercrombie RE (2021) Resolution and uncertainties in estimates of earthquake stress drop and energy release. *Phil Trans R Soc A* 379:20200131. <https://doi.org/10.1098/rsta.2020.0131>
- Bachura M, Fischer T (2019) Waveform cross-correlation for differential time measurement: bias and limitations. *Seismol Res Lett* 90:2005–2014. <https://doi.org/10.1785/0220190096>
- Ben-Zion Y (1998) Properties of seismic fault zone waves and their utility for imaging low-velocity structures. *J Geophys Res* 103:12567–12585. <https://doi.org/10.1029/98JB00768>
- Brune JN (1970) Tectonic stress and the spectra of seismic shear waves from earthquakes. *J Geophys Res* 1977(75):4997–5009. <https://doi.org/10.1029/JB075i026p04997>
- Brune JN (1971) Correction to “Tectonic stress and the spectra, of seismic shear waves from earthquakes.” *J Geophys Res* (1896–1977) 76:5002–5002. <https://doi.org/10.1029/JB076i020p05002>
- Calderoni G, Abercrombie RE (2023) Investigating spectral estimates of stress drop for small to moderate earthquakes with heterogeneous slip distribution: examples from the 2016–2017 Amatrice earthquake sequence. *JGR Solid Earth* 128:e2022JB025022. <https://doi.org/10.1029/2022JB025022>
- Cesca S, Heimann S, Dahm T (2011) Rapid directivity detection by azimuthal amplitude spectra inversion. *J Seismol* 15:147–164. <https://doi.org/10.1007/s10950-010-9217-4>
- Chai G, Yoo S-H, Rhie J, Kang T-S (2020) Stress-drop scaling of the 2016 Gyeongju and 2017 Pohang earthquake sequences using coda-based methods. *Bull Seismol Soc Am* 110:2047–2057. <https://doi.org/10.1785/0120200132>
- Dieterich J (1994) A constitutive law for rate of earthquake production and its application to earthquake clustering. *J Geophys Res* 99:2601–2618. <https://doi.org/10.1029/93JB02581>
- Dreger DS (2003) TDMT_INV: time domain seismic moment tensor INVersion. In: Lee WHK, Kanamori H, Jennings PC, Kisslinger C (eds) International handbook of earthquake and engineering seismology, vol 81B. Academic Press, San Diego, California, p 1627
- Eshelby JD (1957) The determination of the elastic field of an ellipsoidal inclusion, and related problems. *Proc R Soc Lond A* 241:376–396. <https://doi.org/10.1098/rspa.1957.0133>
- Freed AM (2005) Earthquake triggering by static, dynamic, and postseismic stress transfer. *Annu Rev Earth Planet Sci* 33:335–367. <https://doi.org/10.1146/annurev.earth.33.092203.122505>
- Goldstein P, Snoko A (2005) SAC availability for the IRIS community. Incorporated institutions for seismology data management center electronic newsletter
- Heidbach O, Rajabi M, Cui X et al (2018) The world stress map database release 2016: crustal stress pattern across scales. *Tectonophysics* 744:484–498. <https://doi.org/10.1016/j.tecto.2018.07.007>
- Hong T-K, Lee J, Lee J et al (2023) Unravelling a midcrustal seismogenic fault structure from a seismic sequence and geophysical data: application to the 28 October 2022 M_L 4.1 Goesan earthquake in the central Korean Peninsula. *Geophys J Int* 235:1117–1129. <https://doi.org/10.1093/gji/ggad292>
- Kilb D, Gombert J, Bodin P (2000) Triggering of earthquake aftershocks by dynamic stresses. *Nature* 408:570–574. <https://doi.org/10.1038/35046046>
- Kim SJ, Kim SG (1983) A study on the crustal structure of South Korea by using seismic waves. *J Korean Inst Mining Geol* 16:51–61
- Kim WY, Choi H, Noh M (2010) The 20 January 2007 Odaesan, Korea, earthquake sequence: reactivation of a buried strike-slip fault? *Bull Seismol Soc Am* 100:1120–1137. <https://doi.org/10.1785/0120090069>
- Kim S, Rhie J, Kim G (2011) Forward waveform modeling procedure for 1-D crustal velocity structure and its

- application to the southern Korean Peninsula. *Geophys J Int* 185:453–468. <https://doi.org/10.1111/j.1365-246X.2011.04949.x>
- Kim WY, Park JY, Seo M-S et al (2022) The 14 December 2021 Mw 4.9 offshore Jeju island, Korea, earthquake: seismological observation of an intraplate earthquake provides insight into regional seismotectonics. *Seism Rec* 2:107–117. <https://doi.org/10.1785/0320220012>
- Kim WY, Seo M, Park JY et al (2023) The 28 October 2022 Mw 3.8 Goesan earthquake sequence in Central Korea: stress drop, aftershock triggering, and fault interaction. *Bull Seismol Soc Am* 113:2416–2431. <https://doi.org/10.1785/0120230078>
- Li Y-G, Vernon FL (2001) Characterization of the San Jacinto fault zone near Anza, California, by fault zone trapped waves. *J Geophys Res* 106:30671–30688. <https://doi.org/10.1029/2000JB000107>
- Li Y-G, Leary P, Aki K, Malin P (1990) Seismic trapped modes in the Oroville and San Andreas fault zones. *Science* 249:763–766. <https://doi.org/10.1126/science.249.4970.763>
- Lin J, Stein RS (2004) Stress triggering in thrust and subduction earthquakes and stress interaction between the southern San Andreas and nearby thrust and strike-slip faults: stress triggering and fault interaction. *J Geophys Res* 109:B02303. <https://doi.org/10.1029/2003JB002607>
- Madariaga R (1976) Dynamics of an expanding circular fault. *Bull Seismol Soc Am* 66:639–666. <https://doi.org/10.1785/BSSA0660030639>
- Minson SE, Dreger DS (2008) Stable inversions for complete moment tensors. *Geophys J Int* 174:585–592. <https://doi.org/10.1111/j.1365-246X.2008.03797.x>
- Myers SC, Johannesson G, Hanley W (2007) A Bayesian hierarchical method for multiple-event seismic location: Bayesian stochastic multiple-event location. *Geophys J Int* 171:1049–1063. <https://doi.org/10.1111/j.1365-246X.2007.03555.x>
- Park S, Ishii M (2015) Inversion for rupture properties based upon 3-D directivity effect and application to deep earthquakes in the Sea of Okhotsk region. *Geophys J Int* 203:1011–1025. <https://doi.org/10.1093/gji/ggv352>
- Park S-I (2005) Stratigraphy and geological structures of the Ogcheon supergroup in the Jogok area, Goesan, Korea. Seoul National University
- Parsons T (2005) A hypothesis for delayed dynamic earthquake triggering. *Geophys Res Lett* 32:L04302. <https://doi.org/10.1029/2004GL021811>
- Ree J-H, Kim K-H, Lim H et al (2021) Fault reactivation and propagation during the 2017 Pohang earthquake sequence. *Geothermics* 92:102048. <https://doi.org/10.1016/j.geothermics.2021.102048>
- Rhee H, Sheen D (2016) Lateral variation in the source parameters of earthquakes in the Korean Peninsula. *Bull Seismol Soc Am* 106:2266–2274. <https://doi.org/10.1785/0120160085>
- Ross ZE, Ben-Zion Y (2015) An algorithm for automated identification of fault zone trapped waves. *Geophys J Int* 202:933–942. <https://doi.org/10.1093/gji/ggv197>
- Schaff DP, Richards PG (2004) Lg-wave cross correlation and double-difference location: application to the 1999 Xiuyan, China, sequence. *Bull Seismol Soc Am* 94:867–879. <https://doi.org/10.1785/0120030136>
- Shearer PM, Abercrombie RE, Trugman DT, Wang W (2019) Comparing EGF methods for estimating corner frequency and stress drop from *P* wave spectra. *JGR Solid Earth* 124:3966–3986. <https://doi.org/10.1029/2018JB016957>
- Sheen D-H (2021) Analysis of the 2020 Haenam, Korea, earthquake sequence. *Geosci J* 25:33–42. <https://doi.org/10.1007/s12303-020-0038-3>
- Sheen D-H, Seo KJ, Kim S et al (2023) A rapid and automatic procedure for seismic analysis based on deep learning and template matching: a case study on the M 4.1 Goesan earthquake on October 29, 2022. *JGSK* 59:345–354. <https://doi.org/10.14770/jgsk.2023.010>
- Snoke JA (1987) Stable determination of (Brune) stress drops. *Bull Seismol Soc Am* 77:530–538. <https://doi.org/10.1785/BSSA0770020530>
- Snoke JA (2003) FOCMEC: FOCal MECHANism determinations. In: Lee WHK, Kanamori H, Jennings PC, Kisslinger C (eds) *International handbook of earthquake and engineering seismology (Part B)*. Academic Press, San Diego, pp 1629–1630. [https://doi.org/10.1016/S0074-6142\(03\)80291-7](https://doi.org/10.1016/S0074-6142(03)80291-7)
- Soh I, Chang C, Lee J et al (2018) Tectonic stress orientations and magnitudes, and friction of faults, deduced from earthquake focal mechanism inversions over the Korean Peninsula. *Geophys J Int* 213:1360–1373. <https://doi.org/10.1093/gji/ggy061>
- Son M, Shin JS, Kim G, Cho CS (2015) Epicenter relocation of two 2013 earthquake sequences in the Yellow Sea, Korea, using travel-time double-differences and Lg-wave cross-correlation. *Geosci J* 19:295–303. <https://doi.org/10.1007/s12303-014-0038-2>
- Son M, Cho CS, Shin JS et al (2018) Spatiotemporal distribution of events during the first three months of the 2016 Gyeongju, Korea, earthquake sequence. *Bull Seismol Soc Am* 108:210–217. <https://doi.org/10.1785/0120170107>
- Son M, Cho CS, Lee HK et al (2020) Partitioned fault movement and aftershock triggering: evidence for fault interactions during the 2017 Mw 5.4 Pohang earthquake, South Korea. *J Geophys Res Solid Earth* 125:e2020JB020005. <https://doi.org/10.1029/2020JB020005>
- Tape C, Holtkamp S, Silwal V et al (2018) Earthquake nucleation and fault slip complexity in the lower crust of central Alaska. *Nat Geosci* 11:536–541. <https://doi.org/10.1038/s41561-018-0144-2>
- Uchide T, Song SG (2018) Fault rupture model of the 2016 Gyeongju, South Korea, earthquake and its implication for the underground fault system. *Geophys Res Lett* 45:2257–2264. <https://doi.org/10.1002/2017GL076960>
- Waldhauser F, Ellsworth WL (2000) A double-difference earthquake location algorithm: method and application to the northern Hayward Fault, California. *Bull Seismol Soc Am* 90:1353–1368. <https://doi.org/10.1785/0120000006>
- Wessel P, Luis JF, Uieda L et al (2019) The generic mapping tools version 6. *Geochem Geophys Geosyst* 20:5556–5564. <https://doi.org/10.1029/2019GC008515>

Publisher's Note Springer Nature remains neutral with regard to jurisdictional claims in published maps and institutional affiliations.